Multiparticle azimuthal correlations for extracting event-by-event elliptic and triangular flow in Au + Au collisions at sqrt[s_{NN}]=200 GeV

A. Adare *et al.* (PHENIX Collaboration

)

Phys. Rev. C **99**, 024903 — Published 6 February 2019

DOI: 10.1103/PhysRevC.99.024903

Multi-particle azimuthal correlations for extracting event-by-event elliptic and triangular flow in Au+Au collisions at $\sqrt{s_{NN}} = 200$ GeV

A. Adare,[13] C. Aidala,[41] N.N. Ajitanand,[58,*] Y. Akiba,[53,54,†] M. Alfred,[23] N. Apadula,[28,59] H. Asano,[34,53] B. Azmoun,[7] V. Babintsev,[24] A. Bagoly,[17] M. Bai,[6] N.S. Bandara,[40] B. Bannier,[59] K.N. Barish,[8] S. Bathe,[5,54] A. Bazilevsky,[7] M. Beaumier,[8] S. Beckman,[13] R. Belmont,[13,41,47] A. Berdnikov,[56] Y. Berdnikov,[56] D.S. Blau,[33,44] M. Boer,[36] J.S. Bok,[46] K. Boyle,[54] M.L. Brooks,[36] J. Bryslawskyj,[5,8] V. Bumazhnov,[24] S. Campbell,[14,28] V. Canoa Roman,[59] C.-H. Chen,[54] C.Y. Chi,[14] M. Chiu,[7] I.J. Choi,[25] J.B. Choi,[10,*] T. Chujo,[62] Z. Citron,[64] M. Connors,[21,54] M. Csanád,[17] T. Csörgő,[18,65] T.W. Danley,[48] A. Datta,[45] M.S. Daugherity,[1] G. David,[7,59] K. DeBlasio,[45] K. Dehmelt,[59] A. Denisov,[24] A. Deshpande,[54,59] E.J. Desmond,[7] A. Dion,[59] P.B. Diss,[39] J.H. Do,[66] A. Drees,[59] K.A. Drees,[6] J.M. Durham,[36] A. Durum,[24] A. Enokizono,[53,55] S. Esumi,[62] B. Fadem,[42] W. Fan,[59] N. Feege,[59] D.E. Fields,[45] M. Finger,[9] M. Finger, Jr.,[9] S.L. Fokin,[33] J.E. Frantz,[48] A. Franz,[7] A.D. Frawley,[20] C. Gal,[59] P. Gallus,[15] P. Garg,[3,59] H. Ge,[59] F. Giordano,[25] A. Glenn,[35] Y. Goto,[53,54] N. Grau,[2] S.V. Greene,[63] M. Grosse Perdekamp,[25] T. Gunji,[12] T. Hachiya,[43,53,54] J.S. Haggerty,[7] K.I. Hahn,[19] H. Hamagaki,[12] H.F. Hamilton,[1] S.Y. Han,[19] J. Hanks,[59] S. Hasegawa,[29] T.O.S. Haseler,[21] K. Hashimoto,[53,55] X. He,[21] T.K. Hemmick,[59] J.C. Hill,[28] K. Hill,[13] A. Hodges,[21] R.S. Hollis,[8] K. Homma,[22] B. Hong,[32] T. Hoshino,[22] N. Hotvedt,[28] J. Huang,[7] S. Huang,[63] K. Imai,[29] M. Inaba,[62] A. Iordanova,[8] D. Isenhower,[1] D. Ivanishchev,[52] B.V. Jacak,[59] M. Jezghani,[21] Z. Ji,[59] J. Jia,[7,58] X. Jiang,[36] B.M. Johnson,[7,21] D. Jouan,[50] D.S. Jumper,[25] S. Kanda,[12] J.H. Kang,[66] D. Kawall,[40] A.V. Kazantsev,[33] J.A. Key,[45] V. Khachatryan,[59] A. Khanzadeev,[52] C. Kim,[32] D.J. Kim,[30] E.-J. Kim,[10] G.W. Kim,[19] M. Kim,[57] B. Kimelman,[42] D. Kincses,[17] E. Kistenev,[7] R. Kitamura,[12] J. Klatsky,[20] D. Kleinjan,[8] P. Kline,[59] T. Koblesky,[13] B. Komkov,[52] D. Kotov,[52,56] B. Kurgyis,[17] K. Kurita,[55] M. Kurosawa,[53,54] Y. Kwon,[66] R. Lacey,[58] J.G. Lajoie,[28] A. Lebedev,[28] S. Lee,[66] S.H. Lee,[28,59] M.J. Leitch,[36] Y.H. Leung,[59] N.A. Lewis,[41] X. Li,[11] X. Li,[36] S.H. Lim,[36,66] M.X. Liu,[36] S. Lökös,[17,18] D. Lynch,[7] T. Majoros,[16] Y.I. Makdisi,[6] M. Makek,[67] A. Manion,[59] V.I. Manko,[33] E. Mannel,[7] M. McCumber,[36] P.L. McGaughey,[36] D. McGlinchey,[13,36] C. McKinney,[25] A. Meles,[46] M. Mendoza,[8] A.C. Mignerey,[39] D.E. Mihalik,[59] A. Milov,[64] D.K. Mishra,[4] J.T. Mitchell,[7] G. Mitsuka,[31,54] S. Miyasaka,[53,61] S. Mizuno,[53,62] A.K. Mohanty,[4] P. Montuenga,[25] T. Moon,[66] D.P. Morrison,[7] S.I. Morrow,[63] T.V. Moukhanova,[33] T. Murakami,[34,53] J. Murata,[53,55] A. Mwai,[58] K. Nagashima,[22] J.L. Nagle,[13] M.I. Nagy,[17] I. Nakagawa,[53,54] H. Nakagomi,[53,62] K. Nakano,[53,61] C. Nattrass,[60] P.K. Netrakanti,[4] T. Niida,[62] S. Nishimura,[12] R. Nouicer,[7,54] T. Novák,[18,65] N. Novitzky,[30,59] A.S. Nyanin,[33] E. O'Brien,[7] C.A. Ogilvie,[28] J.D. Orjuela Koop,[13] J.D. Osborn,[41] A. Oskarsson,[37] K. Ozawa,[31,62] R. Pak,[7] V. Pantuev,[26] V. Papavassiliou,[46] J.S. Park,[57] S. Park,[53,57,59] S.F. Pate,[46] M. Patel,[28] J.-C. Peng,[25] W. Peng,[63] D.V. Perepelitsa,[7,13] G.D.N. Perera,[46] D.Yu. Peressounko,[33] C.E. PerezLara,[59] J. Perry,[28] R. Petti,[7,59] C. Pinkenburg,[7] R. Pinson,[1] R.P. Pisani,[7] M.L. Purschke,[7] P.V. Radzevich,[56] J. Rak,[30] B.J. Ramson,[41] I. Ravinovich,[64] K.F. Read,[49,60] D. Reynolds,[58] V. Riabov,[44,52] Y. Riabov,[52,56] D. Richford,[5] T. Rinn,[28] S.D. Rolnick,[8] M. Rosati,[28] Z. Rowan,[5] J.G. Rubin,[41] J. Runchey,[28] B. Sahlmueller,[59] N. Saito,[31] T. Sakaguchi,[7] H. Sako,[29] V. Samsonov,[44,52] M. Sarsour,[21] S. Sato,[29] B. Schaefer,[63] B.K. Schmoll,[60] K. Sedgwick,[8] R. Seidl,[53,54] A. Sen,[28,60] R. Seto,[8] P. Sett,[4] A. Sexton,[39] D. Sharma,[59] I. Shein,[24] T.-A. Shibata,[53,61] K. Shigaki,[22] M. Shimomura,[28,43] P. Shukla,[4] A. Sickles,[7,25] C.L. Silva,[36] D. Silvermyr,[37,49] B.K. Singh,[3] C.P. Singh,[3] V. Singh,[3] M.J. Skoby,[41] M. Slunečka,[9] M. Snowball,[36] R.A. Soltz,[35] W.E. Sondheim,[36] S.P. Sorensen,[60] I.V. Sourikova,[7] P.W. Stankus,[49] M. Stepanov,[40,*] S.P. Stoll,[7] T. Sugitate,[22] A. Sukhanov,[7] T. Sumita,[53] J. Sun,[59] Z. Sun,[16] J. Sziklai,[65] A. Taketani,[53,54] K. Tanida,[29,54,57] M.J. Tannenbaum,[7] S. Tarafdar,[63,64] A. Taranenko,[44,58] R. Tieulent,[21,38] A. Timilsina,[28] T. Todoroki,[53,54,62] M. Tomášek,[15] C.L. Towell,[1] R. Towell,[1] R.S. Towell,[1] I. Tserruya,[64] Y. Ueda,[22] B. Ujvari,[16] H.W. van Hecke,[36] J. Velkovska,[63] M. Virius,[15] V. Vrba,[15,27] X.R. Wang,[46,54] Y. Watanabe,[53,54] Y.S. Watanabe,[12,31] F. Wei,[46] A.S. White,[41] C.P. Wong,[21] C.L. Woody,[7] M. Wysocki,[49] B. Xia,[48] C. Xu,[46] Q. Xu,[63] L. Xue,[21] S. Yalcin,[59] Y.L. Yamaguchi,[12,54,59] A. Yanovich,[24] J.H. Yoo,[32] I. Yoon,[57] H. Yu,[46,51] I.E. Yushmanov,[33] W.A. Zajc,[14] A. Zelenski,[6] S. Zharko,[56] S. Zhou,[11] and L. Zou[8]

(PHENIX Collaboration)

[1] *Abilene Christian University, Abilene, Texas 79699, USA*
[2] *Department of Physics, Augustana University, Sioux Falls, South Dakota 57197, USA*
[3] *Department of Physics, Banaras Hindu University, Varanasi 221005, India*
[4] *Bhabha Atomic Research Centre, Bombay 400 085, India*
[5] *Baruch College, City University of New York, New York, New York, 10010 USA*
[6] *Collider-Accelerator Department, Brookhaven National Laboratory, Upton, New York 11973-5000, USA*
[7] *Physics Department, Brookhaven National Laboratory, Upton, New York 11973-5000, USA*

[8] *University of California-Riverside, Riverside, California 92521, USA*
[9] *Charles University, Ovocný trh 5, Praha 1, 116 36, Prague, Czech Republic*
[10] *Chonbuk National University, Jeonju, 561-756, Korea*
[11] *Science and Technology on Nuclear Data Laboratory, China Institute of Atomic Energy, Beijing 102413, People's Republic of China*
[12] *Center for Nuclear Study, Graduate School of Science, University of Tokyo, 7-3-1 Hongo, Bunkyo, Tokyo 113-0033, Japan*
[13] *University of Colorado, Boulder, Colorado 80309, USA*
[14] *Columbia University, New York, New York 10027 and Nevis Laboratories, Irvington, New York 10533, USA*
[15] *Czech Technical University, Zikova 4, 166 36 Prague 6, Czech Republic*
[16] *Debrecen University, H-4010 Debrecen, Egyetem tér 1, Hungary*
[17] *ELTE, Eötvös Loránd University, H-1117 Budapest, Pázmány P. s. 1/A, Hungary*
[18] *Eszterházy Károly University, Károly Róbert Campus, H-3200 Gyöngyös, Mátrai út 36, Hungary*
[19] *Ewha Womans University, Seoul 120-750, Korea*
[20] *Florida State University, Tallahassee, Florida 32306, USA*
[21] *Georgia State University, Atlanta, Georgia 30303, USA*
[22] *Hiroshima University, Kagamiyama, Higashi-Hiroshima 739-8526, Japan*
[23] *Department of Physics and Astronomy, Howard University, Washington, DC 20059, USA*
[24] *IHEP Protvino, State Research Center of Russian Federation, Institute for High Energy Physics, Protvino, 142281, Russia*
[25] *University of Illinois at Urbana-Champaign, Urbana, Illinois 61801, USA*
[26] *Institute for Nuclear Research of the Russian Academy of Sciences, prospekt 60-letiya Oktyabrya 7a, Moscow 117312, Russia*
[27] *Institute of Physics, Academy of Sciences of the Czech Republic, Na Slovance 2, 182 21 Prague 8, Czech Republic*
[28] *Iowa State University, Ames, Iowa 50011, USA*
[29] *Advanced Science Research Center, Japan Atomic Energy Agency, 2-4 Shirakata Shirane, Tokai-mura, Naka-gun, Ibaraki-ken 319-1195, Japan*
[30] *Helsinki Institute of Physics and University of Jyväskylä, P.O.Box 35, FI-40014 Jyväskylä, Finland*
[31] *KEK, High Energy Accelerator Research Organization, Tsukuba, Ibaraki 305-0801, Japan*
[32] *Korea University, Seoul 02841, Korea*
[33] *National Research Center "Kurchatov Institute", Moscow, 123098 Russia*
[34] *Kyoto University, Kyoto 606-8502, Japan*
[35] *Lawrence Livermore National Laboratory, Livermore, California 94550, USA*
[36] *Los Alamos National Laboratory, Los Alamos, New Mexico 87545, USA*
[37] *Department of Physics, Lund University, Box 118, SE-221 00 Lund, Sweden*
[38] *IPNL, CNRS/IN2P3, Univ Lyon, Universit Lyon 1, F-69622, Villeurbanne, France*
[39] *University of Maryland, College Park, Maryland 20742, USA*
[40] *Department of Physics, University of Massachusetts, Amherst, Massachusetts 01003-9337, USA*
[41] *Department of Physics, University of Michigan, Ann Arbor, Michigan 48109-1040, USA*
[42] *Muhlenberg College, Allentown, Pennsylvania 18104-5586, USA*
[43] *Nara Women's University, Kita-uoya Nishi-machi Nara 630-8506, Japan*
[44] *National Research Nuclear University, MEPhI, Moscow Engineering Physics Institute, Moscow, 115409, Russia*
[45] *University of New Mexico, Albuquerque, New Mexico 87131, USA*
[46] *New Mexico State University, Las Cruces, New Mexico 88003, USA*
[47] *Physics and Astronomy Department, University of North Carolina at Greensboro, Greensboro, North Carolina 27412, USA*
[48] *Department of Physics and Astronomy, Ohio University, Athens, Ohio 45701, USA*
[49] *Oak Ridge National Laboratory, Oak Ridge, Tennessee 37831, USA*
[50] *IPN-Orsay, Univ. Paris-Sud, CNRS/IN2P3, Université Paris-Saclay, BP1, F-91406, Orsay, France*
[51] *Peking University, Beijing 100871, People's Republic of China*
[52] *PNPI, Petersburg Nuclear Physics Institute, Gatchina, Leningrad region, 188300, Russia*
[53] *RIKEN Nishina Center for Accelerator-Based Science, Wako, Saitama 351-0198, Japan*
[54] *RIKEN BNL Research Center, Brookhaven National Laboratory, Upton, New York 11973-5000, USA*
[55] *Physics Department, Rikkyo University, 3-34-1 Nishi-Ikebukuro, Toshima, Tokyo 171-8501, Japan*
[56] *Saint Petersburg State Polytechnic University, St. Petersburg, 195251 Russia*
[57] *Department of Physics and Astronomy, Seoul National University, Seoul 151-742, Korea*
[58] *Chemistry Department, Stony Brook University, SUNY, Stony Brook, New York 11794-3400, USA*
[59] *Department of Physics and Astronomy, Stony Brook University, SUNY, Stony Brook, New York 11794-3800, USA*
[60] *University of Tennessee, Knoxville, Tennessee 37996, USA*
[61] *Department of Physics, Tokyo Institute of Technology, Oh-okayama, Meguro, Tokyo 152-8551, Japan*
[62] *Tomonaga Center for the History of the Universe, University of Tsukuba, Tsukuba, Ibaraki 305, Japan*
[63] *Vanderbilt University, Nashville, Tennessee 37235, USA*
[64] *Weizmann Institute, Rehovot 76100, Israel*
[65] *Institute for Particle and Nuclear Physics, Wigner Research Centre for Physics, Hungarian Academy of Sciences (Wigner RCP, RMKI) H-1525 Budapest 114, POBox 49, Budapest, Hungary*
[66] *Yonsei University, IPAP, Seoul 120-749, Korea*
[67] *Department of Physics, Faculty of Science, University of Zagreb, Bijenička c. 32 HR-10002 Zagreb, Croatia*

(Dated: December 7, 2018)

We present measurements of elliptic and triangular azimuthal anisotropy of charged particles detected at forward rapidity $1 < |\eta| < 3$ in Au+Au collisions at $\sqrt{s_{NN}} = 200$ GeV, as a function of centrality. The multiparticle cumulant technique is used to obtain the elliptic flow coefficients $v_2\{2\}$, $v_2\{4\}$, $v_2\{6\}$, and $v_2\{8\}$, and triangular flow coefficients $v_3\{2\}$ and $v_3\{4\}$. Using the small-variance limit, we estimate the mean and variance of the event-by-event v_2 distribution from $v_2\{2\}$ and $v_2\{4\}$. In a complementary analysis, we also use a folding procedure to study the distributions of v_2 and v_3 directly, extracting both the mean and variance. Implications for initial geometrical fluctuations and their translation into the final state momentum distributions are discussed.

* Deceased
† PHENIX Spokesperson: akiba@rcf.rhic.bnl.gov

I. INTRODUCTION

Collisions of heavy nuclei at ultra-relativistic energies are believed to create a state of matter called the strongly coupled quark-gluon plasma, as first observed at the Relativistic Heavy Ion Collider (RHIC) [1–4]. The quark-gluon plasma evolves hydrodynamically as a nearly perfect liquid as evinced by the wealth of experimental measurements and theoretical predictions (or descriptions) of the azimuthal anisotropy of the produced particles. [5]. Multi-particle correlations are generally taken as strong evidence of hydrodynamical flow, which necessarily affects most or all particles in the event [6]. This is different from mimic correlations (generically called nonflow) that are not related to the hydrodynamical evolution and typically involve only a few particles.

Multi-particle correlations are also interesting because they have different sensitivities to the underlying event-by-event fluctuations, which can provide additional insights into the initial geometry and its translation into final state particle distributions [7, 8].

Recently, experimental and theoretical efforts have been directed towards measuring the fluctuations directly, using event-by-event unfolding techniques. In principle, the multi-particle correlations and unfolding techniques provide the same information about the underlying fluctuations, though in practice with different sensitivities [9]. The techniques used at the Large Hadron Collider (LHC) are experimentally very different and provide complementary information [10, 11].

In this manuscript we present measurements of 2-, 4-, 6-, and 8-particle correlations as well as event-by-event measurements of the azimuthal anisotropy parameters corresponding to elliptic v_2 and triangular v_3 flow. We estimate the relationship between the mean and variance with both techniques and discuss the implications for understanding the detailed shape of the v_2 and v_3 distributions. These measurements, while the first of their kind at forward rapidity, are consistent with previous measurements at midrapidity by STAR [12] and PHOBOS [13].

II. EXPERIMENTAL SETUP

In 2014, the PHENIX experiment [14] at RHIC collected nearly 2×10^{10} minimum bias (MB) events of Au+Au collisions at a nucleon-nucleon center-of-mass energy $\sqrt{s_{NN}} = 200$ GeV. The present analysis makes use of a subset ($\approx 10^9$ events) of the total 2014 data sample. The PHENIX beam-beam counters (BBC) are used for triggering and centrality determination. The BBCs [15] are located $\pm$ 144 cm from the nominal interaction point and cover the full azimuth and $3.1 < |\eta| < 3.9$ in pseudorapidity. By convention, the north side is forward rapidity ($\eta > 0$) and the south side is backward rapidity ($\eta < 0$). Each BBC comprises an array of 64 phototubes with a fused quartz Čerenkov radiator on the front. Charged particles impinging on the radiator produce Čerenkov light which is then amplified and detected by the phototube. The PHENIX MB trigger for the 2014 data sample of Au+Au collisions at $\sqrt{s_{NN}} = 200$ GeV was defined by at least two phototubes in each side of the BBC having signal above threshold and an online z-vertex within $\pm$ 10 cm of the nominal interaction point. Additionally, PHENIX has a set of zero-degree calorimeters (ZDC) that measure spectator neutrons from each incoming nucleus [15]. We require a minimum energy in both ZDCs to remove beam related background present at the highest luminosities.

The centrality definition is based on the combined signal in the north and south BBCs. The charge distribution is fitted using a Monte Carlo (MC) Glauber [16] simulation to estimate the number of participating nucleons ($N_{\rm part}$) and a negative binomial distribution to describe the BBC signal for fixed $N_{\rm part}$. All quantities in the present manuscript are reported as a function of centrality and the corresponding $N_{\rm part}$ values are shown in Table I.

The main detector used in the analysis is the forward silicon vertex detector (FVTX). The FVTX [17] is a silicon strip detector comprising two arms, north and south, covering $1 < |\eta| < 3$. In Au+Au collisions there is a strong correlation between the total signal in the BBCs and the total number of tracks in the FVTX. To remove beam related background, we apply an additional event selection on the correlation between the total BBC signal and the number of tracks in the FVTX.

Each FVTX arm has four layers. In the track reconstruction software, a minimum of three hits is required to reconstruct a track. However, it is possible for there to be hit sharing with the central rapidity detector (VTX), so that one or two of the three required hits can be in the VTX. We select tracks using a stricter requirement of at least three hits in FVTX, irrespective of the number of hits in the VTX. We further require that the track reconstruction algorithm have a goodness of fit of χ^2/d.o.f. < 5 for each track. Lastly, we require that each track has a distance of closest approach (DCA) of less than 2 cm. The DCA is defined as the distance between the event vertex and the straight-line extrapolation point of the FVTX track onto a plane which is perpendicular to the z-axis and contains the event vertex. A 2 cm cut selects the FVTX tracks that likely originate from the event vertex, and is conservative in accepting the nonzero DCA tail that stems from the uncertainty in the determination of the vertex position and the bending of the actual track in the experimental magnetic field. Due to the orientation of the FVTX strips relative to the magnetic field, momentum determination is not possible using the tracks in the FVTX alone. However,

TABLE I. $N_{\rm part}$ values for various centrality categories.

Centrality	$\langle N_{\rm part} \rangle$
0%–5%	350.8 ± 3.1
5%–10%	301.7 ± 4.7
10%–20%	236.1 ± 3.8
20%–30%	167.6 ± 5.5
30%–40%	115.5 ± 5.8
40%–50%	76.1 ± 5.5
50%–60%	47.0 ± 4.7
60%–70%	26.7 ± 3.6
70%–80%	13.6 ± 2.4
80%–93%	6.1 ± 1.3

GEANT-4 [18] simulations have determined that the tracking efficiency is relatively independent of momentum for $p_T \gtrsim 0.3$ GeV/c. Figure 1 shows the p_T dependence of the FVTX tracking efficiency averaged over $1 < |\eta| < 3$. Figure 2 shows the tracking efficiency as a function of η in the FVTX for two different z-vertex selections. The single particle tracking efficiency has a maximum value of 98.6% as a function of η. When averaging over $1 < |\eta| < 3$, the maximum value of the p_T-dependent efficiency is 67.9%, and $p_T = 0.3$ GeV/c the efficiency is at 75% of its maximum value.

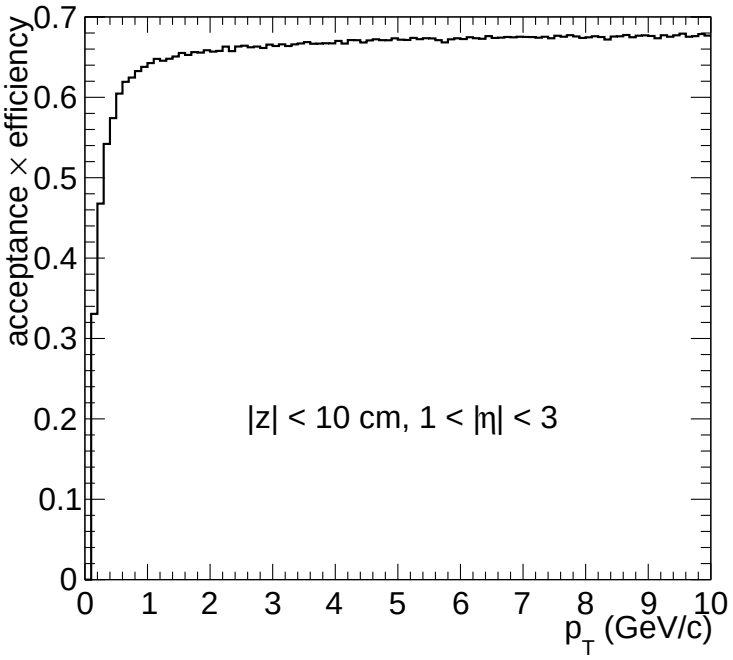

FIG. 1. Tracking efficiency and acceptance in the FVTX as a function of p_T. At $p_T = 0.3$ GeV/c the efficiency is 75% of its asymptotic value.

III. ANALYSIS METHODS

The azimuthal distribution of particles in an event can be represented by a Fourier series [19]:

$$\frac{dN}{d\phi} \propto 1 + \sum_n 2v_n \cos(n(\phi - \psi_n)), \tag{1}$$

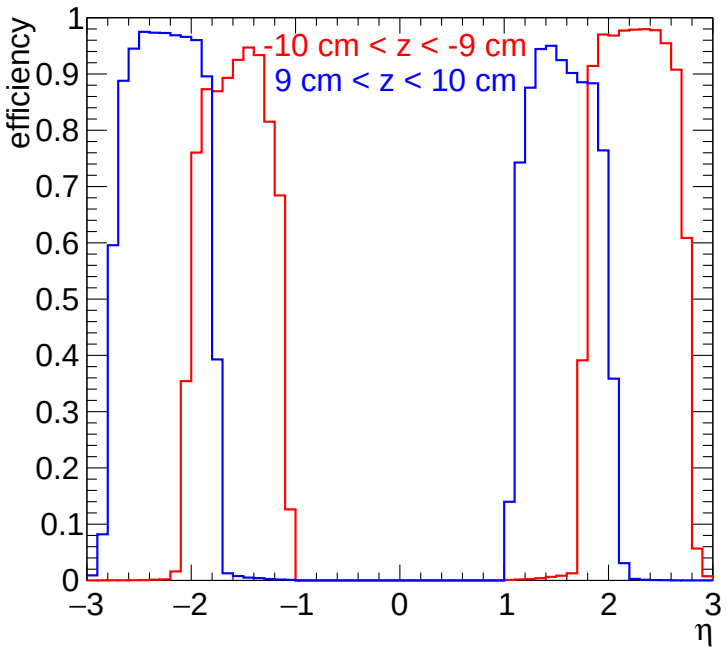

FIG. 2. Tracking efficiency in the FVTX as a function of η for two different z-vertex selections.

where n is the harmonic number, ϕ is the azimuthal angle of some particle, ψ_n is the symmetry plane, and $v_n = \langle\cos(n(\phi-\psi_n))\rangle$. There are many experimental techniques for estimating the v_n coefficients, some of which we discuss in this section.

The main ingredient in the present analysis, for both the cumulant results and the folding results, is the Q-vector. The Q-vector is a complex number $Q_n = Q_{n,x} + iQ_{n,y}$ with the components defined as

$$\Re Q_n = Q_{n,x} = \sum_i^N \cos n\phi_i, \tag{2}$$

$$\Im Q_n = Q_{n,y} = \sum_i^N \sin n\phi_i, \tag{3}$$

where ϕ_i is the azimuthal angle of some particle and N is the number of particles in some event or subevent—a subevent is a subset of a whole event, usually selected based on some kinematic selection, e.g. pseudorapidity. Because the PHENIX FVTX detector subsystem is split into two separate arms, north ($1 < \eta < 3$) and south ($-3 < \eta < -1$), it is natural to use tracks in the two arms as separate subevents for some calculations. In other calculations, all tracks from north and south will be combined into a single event.

Additional corrections to the data are needed to account for any nonuniformity in the azimuthal acceptance. In the case of uniform azimuthal acceptance, the event average of the Q-vector components is zero: $\langle Q_{n,x}\rangle = \langle Q_{n,y}\rangle = 0$. In the case of nonuniform acceptance, there can be a systematic bias such that this relation does not hold. In the case of few-particle correlations, i.e. 2- and 4-particle correlations, the bias can be corrected analytically in a straightforward manner [20]. In the case of correlations with a larger number of particles, however, this becomes impractical. The total number of terms in a k-particle cumulant calculation without the assumption of azimuthal uniformity is given by the Bell sequence: $1, 2, 5, 15, 52, 203, 877, 4140, ...$—that is, the number of terms for 2- and 4-particle correlations is a rather manageable 2 and 15, respectively; contrariwise, the number of terms for 6- and 8-particle correlations is a rather unmanageable 203 and 4140 terms, respectively. For that reason, the only practicable choice is to perform calculations on corrected Q-vectors. The present analysis makes use of Q-vector re-centering [21]. In this procedure one has the relation

$$Q_n^{\text{corrected}} = Q_n^{\text{raw}} - Q_n^{\text{average}}, \tag{4}$$

where

$$Q_n^{\rm average} = N\langle\cos n\phi\rangle + iN\langle\sin n\phi\rangle, \tag{5}$$

and

$$\langle\cos n\phi\rangle = \langle Q_{n,x}/N\rangle, \tag{6}$$
$$\langle\sin n\phi\rangle = \langle Q_{n,y}/N\rangle. \tag{7}$$

In the present analysis, we perform the Q-vector re-centering procedure for each FVTX arm separately and as a function of $N_{\rm tracks}^{\rm FVTX}$. To assess the associated systematic uncertainty, we perform the Q-vector re-centering as a function of centrality instead, as a function of additional secondary variables (event vertex and operational time period), and for combined arms instead of separate.

A. Cumulants

The cumulant method for flow analysis was first proposed in Ref. [22]. In the present analysis, we use the recursion algorithm developed in Ref. [23], which is a generalization of the direct calculations using Q-vector algebra first derived in Ref. [20]. We consider 2-, 4-, 6-, and 8- particle correlations. The multi-particle correlations are denoted $\langle k\rangle$ for k-particle correlations and are estimators for the k-th moment of v_n, i.e. $\langle k\rangle = \langle v_n^k\rangle$. In terms of the angular relationships between different particles, they are

$$\langle 2\rangle = \langle\cos(n(\phi_1 - \phi_2))\rangle, \tag{8}$$
$$\langle 4\rangle = \langle\cos(n(\phi_1 + \phi_2 - \phi_3 - \phi_4))\rangle, \tag{9}$$
$$\langle 6\rangle = \langle\cos(n(\phi_1 + \phi_2 + \phi_3 - \phi_4 - \phi_5 - \phi_6))\rangle, \tag{10}$$
$$\langle 8\rangle = \langle\cos(n(\phi_1 + \phi_2 + \phi_3 + \phi_4 - \phi_5 - \phi_6 - \phi_7 - \phi_8))\rangle, \tag{11}$$

where $\phi_{1,\ldots,8}$ represent the azimuthal angles of different particles in the event.

The k-particle cumulants, denoted $c_n\{k\}$ are constructed in such a way that potential contributions from lower order correlations are removed. Because the cumulants mix various terms that are of equal powers of v_n, the cumulant method v_n, denoted $v_n\{k\}$, is proportional to the k-th root of the cumulant. The $c_n\{k\}$ are constructed as follows:

$$c_n\{2\} = \langle 2\rangle, \tag{12}$$
$$c_n\{4\} = \langle 4\rangle - 2\langle 2\rangle^2, \tag{13}$$
$$c_n\{6\} = \langle 6\rangle - 9\langle 4\rangle\langle 2\rangle + 12\langle 2\rangle^3, \tag{14}$$
$$c_n\{8\} = \langle 8\rangle - 16\langle 6\rangle\langle 2\rangle - 18\langle 4\rangle^2 + 144\langle 4\rangle\langle 2\rangle^2 - 144\langle 2\rangle^4, \tag{15}$$

and the $v_n\{k\}$ are

$$v_n\{2\} = (c_n\{2\})^{1/2}, \tag{16}$$
$$v_n\{4\} = (-c_n\{4\})^{1/4}, \tag{17}$$
$$v_n\{6\} = (c_n\{6\}/4)^{1/6}, \tag{18}$$
$$v_n\{8\} = (-c_n\{8\}/33)^{1/8}. \tag{19}$$

It is also possible to construct cumulants in two or more subevents, though in the present analysis we will only concern ourselves with two subevents. For 2-particle correlations, rather than $\langle 2\rangle = \langle\cos(n(\phi_1 - \phi_2))\rangle$ where ϕ_1 and ϕ_2 are from the same subevent, one has instead $\langle 2\rangle_{a|b} = \langle\cos(n(\phi_1^a - \phi_2^b))\rangle$ where a, b denote two different subevents. The cumulant and v_n have the same relationship as in the single event case, i.e. $v_n\{2\}_{a|b}^2 = c_n\{2\}_{a|b} = \langle 2\rangle_{a|b}$. The two-subevent 2-particle cumulant is also known as the scalar product method [24].

Subevent cumulants for correlations with four or more particles were first proposed in Ref. [25]. For two-subevent 4-particle correlations, there are two possibilities:

$$\langle 4\rangle_{ab|ab} = \langle\cos(n(\phi_1^a + \phi_2^b - \phi_3^a - \phi_4^b))\rangle, \tag{20}$$
$$\langle 4\rangle_{aa|bb} = \langle\cos(n(\phi_1^a + \phi_2^a - \phi_3^b - \phi_4^b))\rangle, \tag{21}$$

where the former allows 2-particle correlations within single subevents and the latter excludes them. The latter is therefore less susceptible to nonflow than the former, although both are less susceptible to nonflow than single event 4-particle correlations. The cumulants take the form

$$c_n\{4\}_{ab|ab} = \langle 4\rangle_{ab|ab} - \langle 2\rangle_{a|a}\langle 2\rangle_{b|b} - \langle 2\rangle^2_{a|b}, \tag{22}$$

$$c_n\{4\}_{aa|bb} = \langle 4\rangle_{aa|bb} - 2\langle 2\rangle^2_{a|b}, \tag{23}$$

and the $v_n\{4\}$ values have the same relationship to the cumulants as in the single particle case, i.e. $v_n\{4\}_{ab|ab} = (-c_n\{4\}_{ab|ab})^{1/4}$ and $v_n\{4\}_{aa|bb} = (-c_n\{4\}_{aa|bb})^{1/4}$.

To determine systematic uncertainties associated with event and track selection for the cumulant analysis, we vary the event and track selection criteria and assess the variation on the final analysis results. The z-vertex selection is modified from $\pm$ 10 cm to $\pm$ 5 cm. The track selections are independently modified to have a goodness of fit requirement χ^2/d.o.f. < 3. These changes move the cumulant results by an almost common multiplicative value and thus we quote the systematic uncertainties as a global scale factor uncertainty for each result.

B. Folding

Here we describe an alternative approach where one utilizes the event-by-event Q_n distribution to extract the event-by-event v_n distribution via an unfolding procedure. For our analysis we attempt a procedure similar to that used by ATLAS as described in Ref. [10].

In brief, ATLAS successfully carries out the unfold in Pb+Pb collisions at 2.76 TeV and finds that the event-by-event probability distribution for elliptic flow $p(v_2)$ is reasonably described by a Bessel-Gaussian function

$$p(v_n) = \frac{v_n}{\delta^2_{v_n}} e^{-\frac{(v_n^2+(v_n^{\rm RP})^2)}{2\delta^2_{v_n}}} I_0\left(\frac{v_n v_n^{\rm RP}}{\delta^2_{v_n}}\right), \tag{24}$$

where $v_n^{\rm RP}$ and $\delta^2_{v_n}$ are function parameters that are related *but not equal* to the mean and variance of the distribution, respectively. Because flow is a vector quantity, it has both a magnitude and a phase. When measuring v_n one measures the modulus of the complex number, meaning there is a reduction in the number of dimensions from two to one. If the fluctuations in each dimension are Gaussian, one then expects the final distribution of values to be Bessel-Gaussian. Recently the CMS experiment has carried out a similar flow unfolding and observes small deviations from the Bessel-Gaussian form, favoring the elliptic power distribution [26].

For the unfolding, ATLAS determines the response matrix in a data driven way. The smearing in the response matrix is modest as Pb+Pb collisions have a high multiplicity and the ATLAS detector has large phase space coverage for tracks $-2.5 < \eta < +2.5$. In our case, the multiplicity of Au+Au collisions is lower in comparison with the multiplicity in Pb+Pb collisions and the phase space coverage of the FVTX detector is significantly smaller. Hence, the smearing as encoded in the response matrix is significantly larger and the unfolding is more challenging.

To estimate the response function of the detector, we follow the procedure from ATLAS [10], which is to examine the difference between two subevents for both Q_x and Q_y. We compare the Q-vector determined in the south arm of the FVTX, $Q^{\rm south}$, to the Q-vector determined in the north arm of the FVTX, $Q^{\rm north}$. Figure 3 shows an example of this procedure for the $n = 2$ case. Figure 3 (a) shows the 2-dimensional distribution for the 20%–30% centrality selection; Fig 3 (b) shows the one-dimensional projection of this onto the x-axis (i.e. the one-dimensional distribution of $Q_x^{\rm north} - Q_x^{\rm south}$); Fig 3 (c) shows the one-dimensional projection of this onto the y-axis (i.e. the one-dimensional distribution of $Q_y^{\rm north} - Q_y^{\rm south}$). These distributions in all centrality selections are Gaussian over four orders of magnitude, and we characterize them via their Gaussian widths δ_{2SE} which are given in Table II. It is notable that these widths are more than a factor of two larger than those quoted by ATLAS in Pb+Pb collisions, for example $\delta_{2SE} = 0.050$ for Pb+Pb 20%–25% central events [10].

If there is a modest longitudinal decorrelation between the two subevents, it will manifest as a slight increase in the δ_{2SE} parameter. The final v_n is averaged over that decorrelation. This effect, as in previous unfolding analyses [10], is neglected.

We highlight that even in the case of a perfect detector with perfect acceptance, there remains a smearing due to the finite particle number in each event. This raises a question regarding the meaning of a true v_n that is being unfolded back to. In a hydrodynamic description, there is a continuous fluid from which one can calculate a single true anisotropy v_n for each event. If one then has the fluid breakup into a finite number of particles N, e.g. via Cooper-Frye freeze-out, the anisotropy of those N particles will fluctuate around the true fluid value. However, in a parton scattering description, for example AMPT [27], the time evolution is described in terms of a finite number of particles N. In this sense there is no separating of a true v_n from that encoded in the N particles themselves.

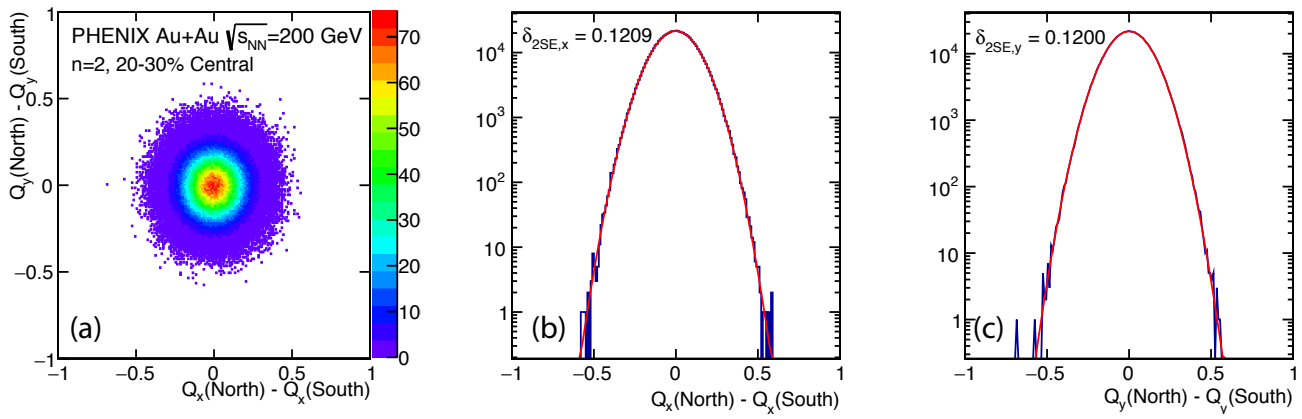

FIG. 3. Example distribution of $Q^{\rm north} - Q^{\rm south}$ for the $n = 2$ case corresponding to Au+Au collisions at $\sqrt{s_{NN}} = 200$ GeV and centrality 20–30%. (a) The two-dimensional distribution. (b) The projection onto Q_x. (c) The projection onto Q_y. Shown for (b) and (c) are the extracted Gaussian widths δ_{2SE}—the χ^2/d.o.f. values of the fits are 1.02 and 1.18 for (b) and (c), respectively.

TABLE II. Resolution parameter δ_{2SE} values for $n = 2$ and $n = 3$ for various centrality categories.

Centrality	$\delta_{2SE}(n = 2)$	$\delta_{2SE}(n = 3)$
0%–5%	0.117	0.115
5%–10%	0.115	0.113
10%–20%	0.115	0.113
20%–30%	0.121	0.119
30%–40%	0.133	0.130
40%–50%	0.154	0.151

Regardless, one can still mathematically apply the unfolding and compare experiment and theory as manipulated through the same algorithm.

As noted before, the one-dimensional radial projection of a two-dimensional Gaussian is the so-called Bessel-Gaussian function. In this case it means that the conditional probability to measure a value $v_n^{\rm obs}$ given a true value v_n has the following Bessel-Gaussian form:

$$p(v_n^{\rm obs}|v_n) \propto v_n^{\rm obs} e^{-\frac{(v_n^{\rm obs})^2+v_n^2}{2\delta^2}} I_0\left(\frac{v_n^{\rm obs} v_n}{\delta^2}\right), \tag{25}$$

where δ is the smearing parameter characterizing the response due to the finite particle number (including from the detector efficiency and acceptance), and I_0 is a modified Bessel function of the first kind. The smearing parameter δ uses the combination of the two FVTX arms and is related to the result from the difference by $\delta = \delta_{2SE}/2$. We highlight that the Bessel-Gaussian in Eqn. 25 is different from the Bessel-Gaussian in Eqn. 24, though both arise from a similar dimensional reduction.

We have employed the iterative Bayes unfold method as encoded in RooUnfold [28] and our own implementation of a Singular Value Decomposition (SVD) unfold method [29, 30]. In both cases, the response matrix is populated using Eqn. 25 using the data-determined smearing parameters. The FVTX-determined event-by-event Q_n distributions are used as input to the unfold. Figure 4 shows this dimensional reduction for the $n = 2$ and $n = 3$ case, respectively. Figure 4 (a) and (c) show the two-dimensional distribution of Q_n and Figure 4 (b) and (d) show the one-dimensional distribution of $|Q_n|$ for the 20%–30% centrality range.

The Au+Au 20%–30% centrality class is expected to provide the best conditions, in terms of the predicted $\langle v_2 \rangle$ and resolution δ, to determine $p(v_2)$ via unfolding. However, because it is quite challenging to unfold the measured distribution directly, we constructed a test version of the problem to illustrate the procedure using the SVD method. The details of this test are given in Appendix V, but the end result is that the unfolding procedure is inherently unstable and therefore fails to converge for the resolution parameters in the present analysis.

As a result, instead of inverting the response matrix, we can make an *ansatz* that the probability distributions,

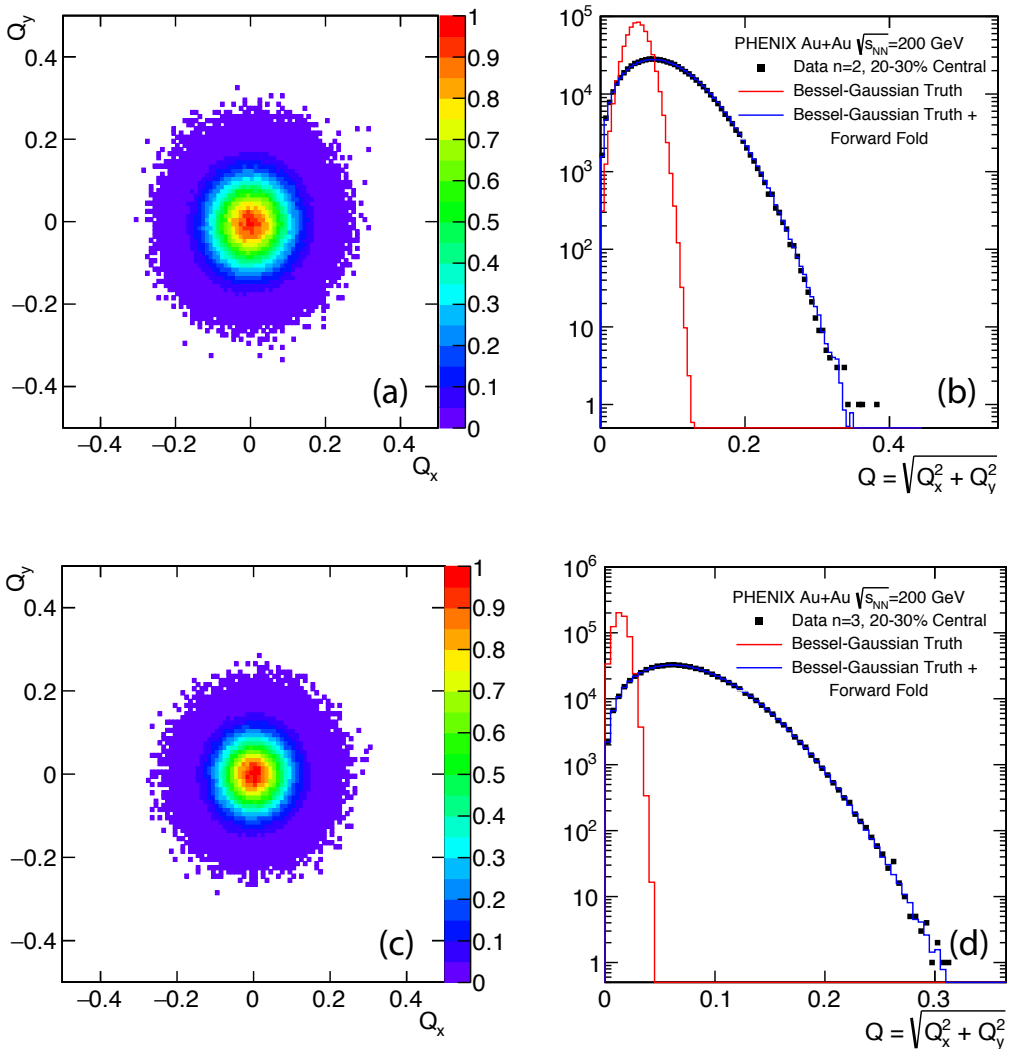

FIG. 4. Example distribution of Q for the (a), (b) elliptic $n = 2$ case and (c), (d) triangular $n = 3$ case (lower). (a) and (c) show the 2-dimensional distribution. (b) and (d) show the 1-dimensional distribution $|Q|$. The distribution corresponds to Au+Au collisions at $\sqrt{s_{NN}} = 200$ GeV and centrality 20–30%. Also shown in (b), (d) is the best fit for this run Bessel-Gaussian truth distribution and the corresponding forward folded result (i.e. pushing the truth distribution through the response matrix).

$p(v_2)$ and $p(v_3)$ are exactly Bessel-Gaussian in form. Under this restrictive assumption, because the Bessel-Gaussian form has only two parameters as shown in Eqn. 24, we can simply evaluate a large grid of parameter combinations as guesses for the truth distribution and forward fold them, i.e. passing them through the response matrix to compare to the observed Q_n distribution. We have carried out such a "forward fold" procedure with over 10,000 parameter combinations. We then determine the statistical best fit parameters and their statistical uncertainties based on a χ^2 mapping. We consider only the Gaussian statistical uncertainties here, and detail our treatment of systematic uncertainties in Section IV B. Some advantages of this procedure are that we explore the full χ^2 space and have no sensitivity to an unfolding prior, regularization scheme, and number of iterations. The disadvantage of course is the *ansatz* that the distribution is precisely Bessel-Gaussian.

Examples of this χ^2 forward fold mapping are shown in Figure 5. It is striking that for the v_2 case in the Au+Au 20%–30% central bin, the forward folding reveals a tight constraint on the Bessel-Gaussian parameters. In contrast, for the same centrality bin and v_3, there is a band of parameter combinations providing a roughly equally good match to the experimental Q_3 distribution. Shown in Figure 4 for v_2 (upper) and v_3 (lower) are the best Bessel-Gaussian fit distributions (red) and their forward folded results (blue). Both cases show good agreement between the forward folded results and the measured experimental distribution. The corresponding best $\chi^2_{\rm min}$ values indicate a good match.

It is notable that in the v_3 case, the $\chi^2_{\rm min}$ values are slightly worse in all cases and significantly worse in the most peripheral selection. The more peripheral data have a slightly larger tail at high Q_3 values which could indicate an incompatibility with the Bessel-Gaussian *ansatz*.

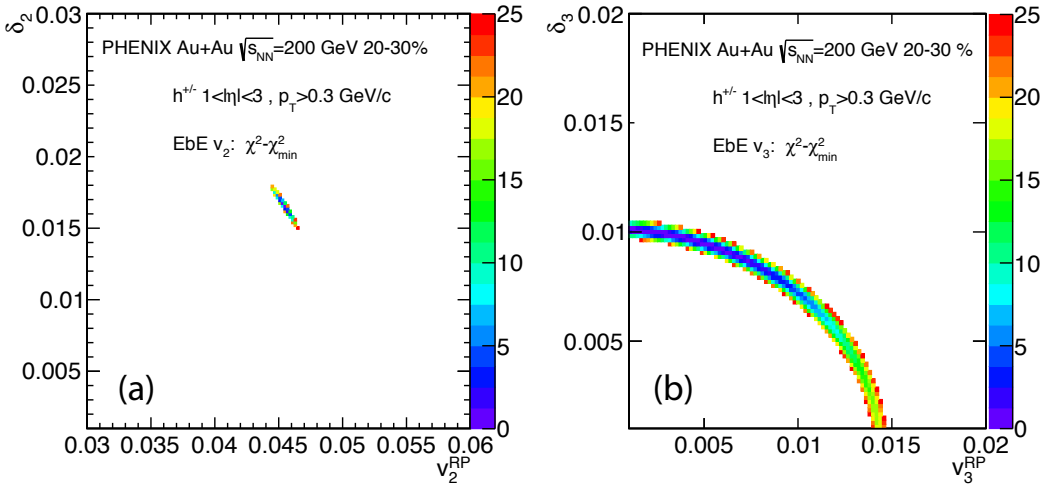

FIG. 5. Two dimensional color plot of $\chi^2 - \chi^2_{\rm min}$ values as a function of the two Bessel-Gaussian parameters, $v_n^{\rm RP}$ and δ_{v_n} for the 20%–30% centrality bin. (a) shows the second harmonic and (b) shows the third harmonic. Only χ^2 values up to $\chi^2_{\rm min}+25$ are shown.

IV. RESULTS AND DISCUSSION

Here we detail the full set of results for the elliptic and triangular flow moments and distributions in Au+Au collisions at $\sqrt{s_{NN}} = 200$ GeV. We start by detailing the cumulant results.

A. Cumulants Results

First we show in Figure 6 (a) and (b) the centrality dependence of $v_2\{2\}$ and $v_2\{4\}$, respectively. The statistical uncertainties are shown as vertical lines and the systematic uncertainty is quoted as a global factor uncertainty. (a) shows a dramatic difference for centrality larger than 40% between the red points, obtained without requiring a pseudorapidity gap in the particle pair, and the magenta points, which have a pseudorapidity gap of $|\Delta\eta| > 2.0$. This is due to the fact that the pseudorapidity gap removes a large amount of nonflow, especially in the peripheral collisions where nonflow is combinatorially less suppressed relative to central collisions. Contrariwise, (b) shows no difference between the black points (no pseudorapidity gap) and two different 2-subevent cumulants, one where short-range pairs are allowed (blue points) and one where they are not (red points). The absence of any effect here indicates that the 4-particle correlation sufficiently suppresses nonflow combinatorially such that the kinematic separation of particles provides no additional benefit. Note that this is not necessarily the case in smaller collision systems—subevent cumulants have been shown to significantly reduce nonflow in p+p/Pb collisions at the LHC [31], and are of potential interest in $p/d/^3$He+Au collisions at RHIC.

Figure 7 shows the centrality dependence of multi-particle v_2, with 2, 4, 6, and 8 particles. The 4-, 6-, and 8-particles v_2 values are consistent with each other, as expected from the small-variance limit [7]. When accounting for the η-dependence of v_2 as measured by PHOBOS [32], which indicates that v_2 at $1 < |\eta| < 3$ is about 1.25 times lower than it is at $|\eta| < 1$, the 2-, 4-, and 6-particle cumulant v_2 are in good agreement with the STAR results [12].

Considering that $v_n\{2\} = \sqrt{v_n^2 + \sigma^2_{v_n}}$ and that in the small variance limit $v_n\{4\} \approx \sqrt{v_n^2 - \sigma^2_{v_n}}$ [8], one can estimate the relative fluctuations as

$$\frac{\sigma_{v_n}}{\langle v_n \rangle} \approx \sqrt{\frac{(v_n\{2\})^2 - (v_n\{4\})^2}{(v_n\{2\})^2 + (v_n\{4\})^2}}. \tag{26}$$

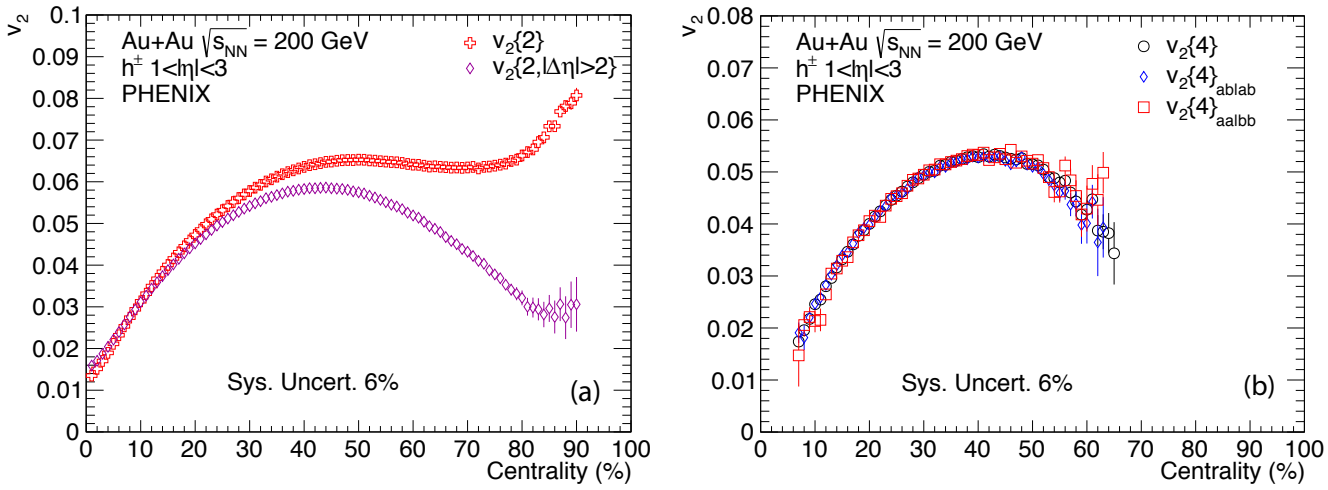

FIG. 6. Centrality dependence of (a) $v_2\{2\}$ and (b) $v_2\{4\}$. (a) The red points indicate no pseudorapidity gap whereas the magenta points indicate a pseudorapidity gap of $|\Delta\eta| > 2.0$. (b) The black points indicate $v_2\{4\}$ with no pseudorapidity gap, the blue points indicate a two-subevent method with $|\Delta\eta| > 2.0$ but where some short-range pairs are allowed, and the red points indicate a two-subevent method with $|\Delta\eta| > 2.0$ where no short-range pairs are allowed.

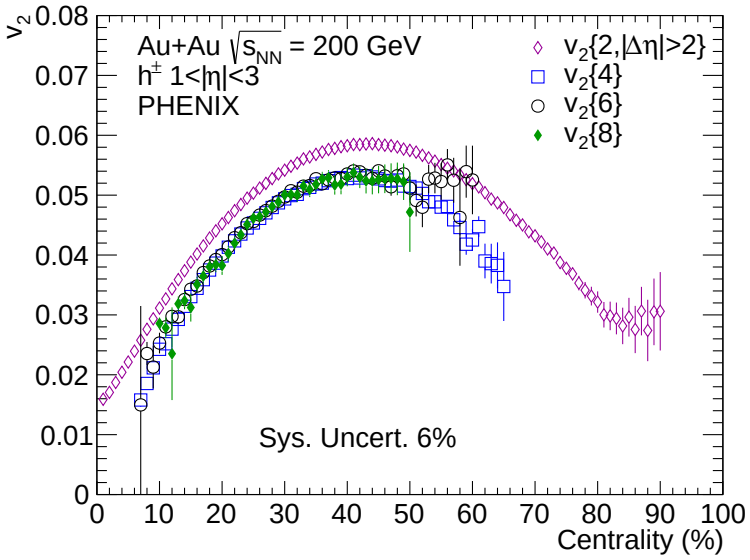

FIG. 7. Multi-particle v_2 as a function of centrality in Au+Au collisions at $\sqrt{s_{NN}} = 200$ GeV. The magenta open diamonds indicate the $v_2\{SP\}$, the blue open squares indicate $v_2\{4\}$, the black open circles indicate $v_2\{6\}$, and the green filled diamonds indicate $v_2\{8\}$.

Figure 8 shows the centrality dependence of this cumulant estimate of $\sigma_{v_2}/\langle v_2\rangle$. Despite the difference in the rapidity region where the data are measured, they are in good agreement with STAR [12] and PHOBOS [13]. Also shown is a comparison with AMPT analyzed via cumulants in the same way as the experimental data. There is good agreement between the two, indicating that the Monte Carlo Glauber initial conditions in AMPT and their fluctuations capture the key event-by-event varying ingredients. We can also calculate the event-by-event variations in the initial conditions directly via Monte Carlo Glauber. In this case we utilize the event-by-event spatial eccentricity ε_n distributions. If there is a linear mapping between initial spatial eccentricity and final momentum anisotropy ($\varepsilon_n \propto v_n$), we should expect a good match between $\sigma_{\varepsilon_n}/\langle\varepsilon_n\rangle$ and $\sigma_{v_n}/\langle v_n\rangle$. Also show in Fig. 8 is the Monte Carlo Glauber result via the calculation of cumulants (solid blue line), as well as the direct calculation of the variance and mean from the full ε_n distribution (dashed blue line). One sees that in midcentral 10%–50% collisions, the data and both theory curves agree reasonably. For more central collisions, the Monte Carlo Glauber data-style calculation shows the same trend

as the data whereas the Monte Carlo Glauber direct calculation is significantly lower. This is due to the fact that the small-variance limit is not a valid approximation in central collisions. In peripheral collisions, both Monte Carlo Glauber curves under-predict the data. This has been attributed to the nonlinear response in hydrodynamics [33].

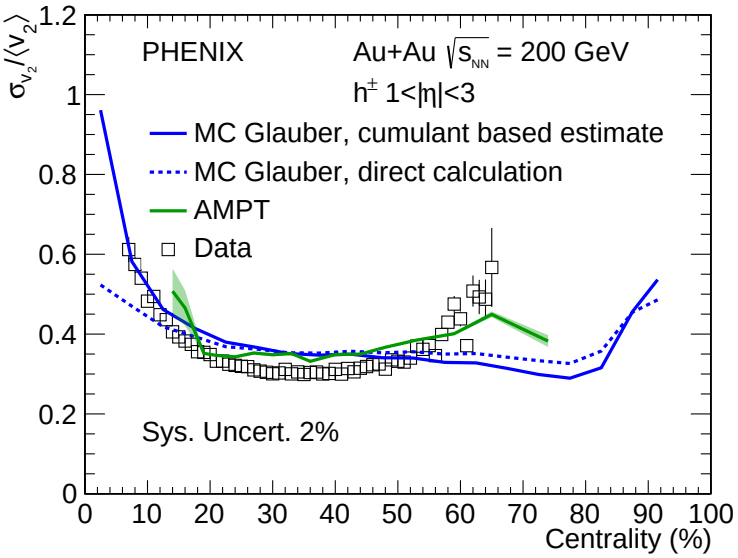

FIG. 8. Cumulant method estimate of $\sigma_{v_2}/\langle v_2 \rangle$ as a function of centrality in Au+Au collisions at $\sqrt{s_{NN}}$ = 200 GeV. The data are shown as black open squares. The same calculation as done in data is done in AMPT, shown as a solid green line. Calculations of $\sigma_{\varepsilon_2}/\langle \varepsilon_2 \rangle$ performed in the Monte Carlo Glauber model are shown as blue lines. The solid blue line is the Monte Carlo Glauber calculation done using the same estimate as the data, the dashed blue line is the direct calculation of the moments of the MC Glauber ε_2 distribution.

Now we consider the v_3 case. Figure 9 shows $v_3\{2, |\Delta\eta| > 2\}$ as a function of centrality. The centrality dependence of v_3 is much smaller than that of v_2, which is expected because triangular flow is generated dominantly through fluctuations.

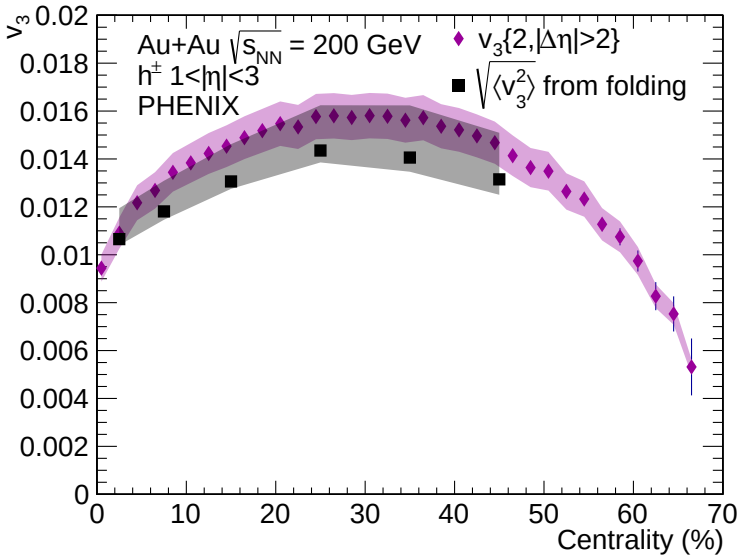

FIG. 9. Centrality dependence of $v_3\{2, |\Delta\eta| > 2\}$ in Au+Au collisions at $\sqrt{s_{NN}}$ = 200 GeV, shown as magenta diamonds. The systematic uncertainty is indicated as a shaded magenta band. Also shown as black squares are $\sqrt{\langle v_3^2 \rangle}$ as determined from the folding analysis, which is shown in the next section.

Figure 10 (a) shows the results for $c_3\{4\}$ as a function of centrality. The results are always positive within the

systematic uncertainties and shows a trend towards even larger positive values as one moves away from the most central collisions. Since $v_3\{4\} = (-c_3\{4\})^{1/4}$ the $v_3\{4\}$ are complex-valued.

Recently positive valued $c_2\{4\}$ has been observed in p+Au collisions at RHIC [34] and p+p collisions at the LHC [31, 35] and has been interpreted as arising from short range nonflow contributions. The use of subevents, especially when requiring the particles in the cumulant to be separated in rapidity, significantly reduces nonflow contributions and yields negative values of $c_2\{4\}$ where standard cumulant analysis does not [25]. In the Au+Au analysis presented here, due to the FVTX acceptance, one includes both short range particle combinations (some or all particles in a single FVTX arm) and long-range combinations.

We explore the potential influence of such short range nonflow contributions as well as the opposite effect from long-range decorrelations by changing the FVTX arm requirements of the particle combinations. The most extreme is requiring all particles in a single arm, shown in Figure 10 (b), and the result is an even larger positive $c_3\{4\}$—i.e. in the direction expected from increased short range nonflow and opposite to the expectation of long-range decorrelations causing the positive $c_3\{4\}$. We can also consider combinations of two subevents, with two particles in each FVTX arm. One case, labeled $ab|ab$, has some short range correlations though fewer than the standard, whereas the other case, labeled $aa|bb$, doesn't allow any. One sees a consistent behavior emerge: $c_3\{4\}_{aa|bb} < c_3\{4\}_{ab|ab} < c_3\{4\} < c_3\{4\}_{\rm singlearm}$ All of these results go in the direction of a large nonflow influence which may be exacerbated by the very small v_3 flow signal particularly, at forward rapidity.

The STAR experiment has also measured $c_3\{4\}$ in Au+Au collisions at $\sqrt{s_{NN}} = 200$ GeV, though at midrapidity $|\eta| < 1.0$ [36]. Their results, also shown in Figure 10 (a), are consistent with zero and fluctuate between positive and negative $c_3\{4\}$ values. The difference between the STAR and PHENIX data points likely stems from the different acceptance in pseudorapidity (the STAR points are measured over $|\eta| < 1$ while the PHENIX points are measured over $1 < |\eta| < 3$ as discussed above). Differences in nonflow, event plane decorrelations, and the relative contribution from fluctuations as a function of pseudorapidity may all contribute to these observations.

These results seem to indicate that the small-variance limit is not applicable to v_3 in Au+Au collisions at $\sqrt{s_{NN}}$ = 200 GeV for any centrality. Regardless, the measurement of these 2- and 4-particle cumulants is insufficient to constrain the mean and variance of the triangular flow event-by-event distribution.

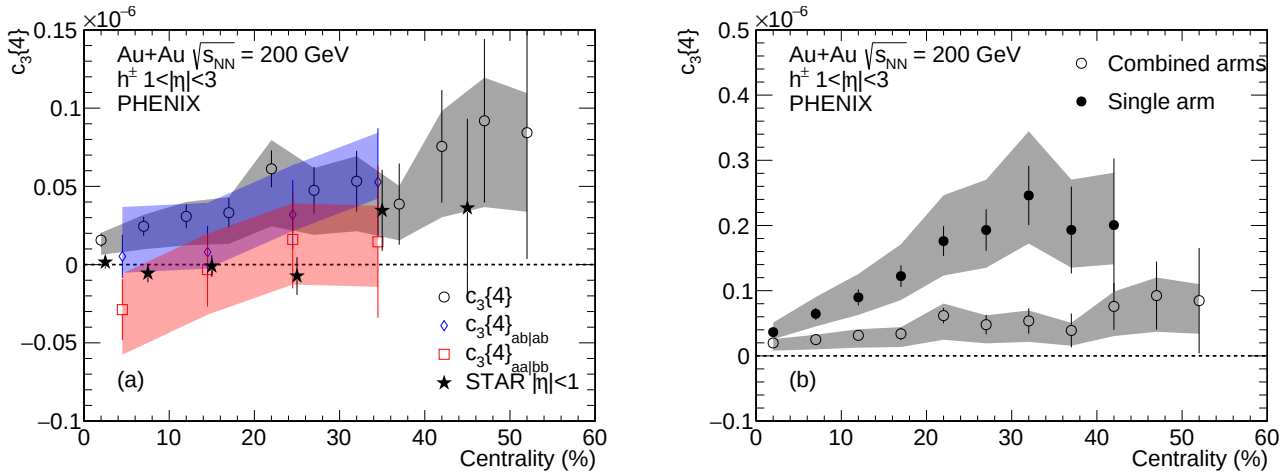

FIG. 10. Centrality dependence of $c_3\{4\}$ for Au+Au collisions at $\sqrt{s_{NN}} = 200$ GeV. (a) Calculations using both arms: $c_3\{4\}$ (black circles), $c_3\{4\}_{ab|ab}$ (blue diamonds), $c_3\{4\}_{aa|bb}$ (red squares), and comparison to STAR [36] (black stars). (b) Comparison of $c_3\{4\}$ determined using both arms (open symbols) and a single arm (closed symbols). Note that the open black circles are the same in (a) and (b).

B. Folding Results

Now we turn to the results from the event-by-event forward fold. As detailed in Section III B, in the v_2 case the Bessel-Gaussian parameters are well-constrained apart from the most central events. In the v_3 case, however, the Bessel-Gaussian parameters are not well-constrained for any centrality class. However, despite the broad range of possible δ_{v_3} and $v_3^{\rm RP}$ values, these correspond to a rather small range for the real mean $\langle v_3 \rangle$ and root-mean-square or variance σ_{v_3} of the distributions. This means that despite the lack of constraint on the parameters, the first (v_3) and second (σ_{v_3}) moments of the distribution are nevertheless well-constrained.

We can quantify $\langle v_n \rangle$ and σ_{v_n} by varying the Bessel-Gaussian parameters within the one- and two- standard deviation statistical constraints. In addition, we determine the systematic uncertainties on these quantities by varying the z-vertex and analyzing loose and tight cuts (as described for the cumulants analysis). An additional systematic uncertainty on the response matrix is estimated by splitting the data sample into two subsets, one with higher extracted δ and one with lower, forward folding the two data sets separately, and then assessing the difference.

Figure 11 (a) shows the extracted first moment $\langle v_2 \rangle$, Fig. 11 (b) shows the extracted second moment σ_{v_2}, and Fig. 11 (c) shows the relative fluctuations $\sigma_{v_2}/\langle v_2 \rangle$, each as determined from the folding method and as a function of centrality. Likewise, Fig. 12 (a) shows the extracted $\langle v_3 \rangle$, Fig. 12 (b) shows the extracted σ_{v_3}, and Fig. 12 (c) shows the relative fluctuations $\sigma_{v_3}/\langle v_3 \rangle$. The colored bands indicate the statistical uncertainties at the 68.27% confidence level (red) and the 95.45% confidence level (green) from the χ^2 analysis. The thin black lines indicate the systematic uncertainties. Also shown in 11 as blue squares are results from the cumulant based calculation as discussed in the previous section. The $\langle v_2 \rangle$ values are in excellent agreement for all centralities, and the σ_{v_2} and $\sigma_{v_2}/\langle v_2 \rangle$ are in reasonable agreement for 10%–50% centrality, where the small-variance limit holds. Figure 9 shows a comparison between the cumulant result $v_3\{2, |\Delta\eta| > 2|\}$ and the folding analysis result $\sqrt{\langle v_3^2 \rangle}$ (calculated from the results in Fig. 12). These results are consistent within the systematic uncertainties.

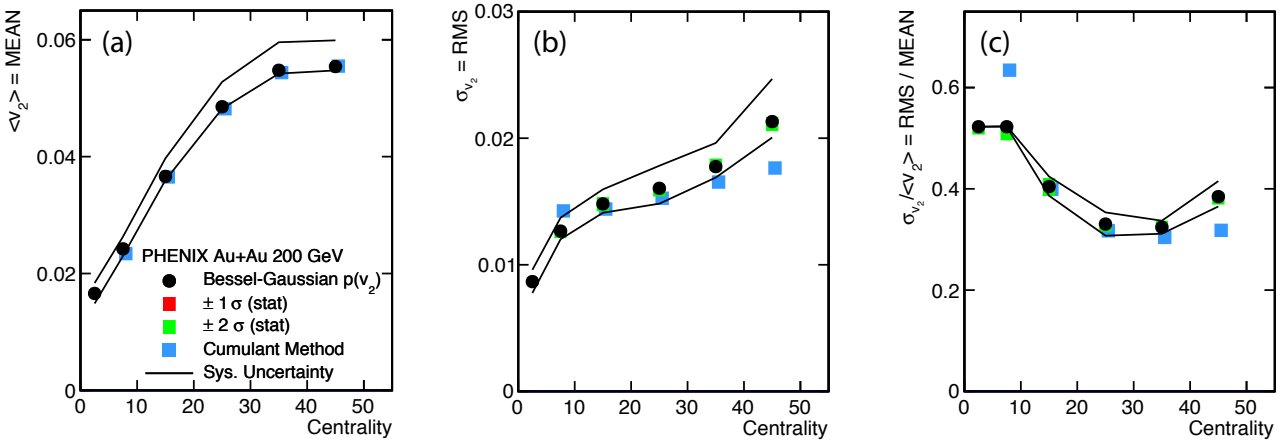

FIG. 11. Folding results for (a) v_2, (b) σ_{v_2}, and (c) $\sigma_{v_2}/\langle v_2 \rangle$. The black lines above and below the points indicate the systematic uncertainties. The red (green) boxes indicate the statistical uncertainties at the 68.27% (95.45%) confidence level. In the case of $\langle v_2 \rangle$, the statistical uncertainties at the 68.27% confidence level are too small to be seen, and the uncertainties at the 95.45% confidence level are visible but noticeably smaller than the marker size. Shown as blue squares are the same quantities as determined using the cumulant based calculation—these points are slightly offset in the x-coordinate to improve visibility.

We highlight that the $\sigma_{v_2}/\langle v_2 \rangle$ values agree well with those determined from the cumulant method as shown in Figure 8, except in the most central and peripheral Au+Au events. The most central 0%–5% events are exactly where the Monte Carlo Glauber results in Figure 8 indicate a breakdown in the small-variance approximation. This is a good validation of the forward folding procedure and another confirmation that the event-by-event elliptic flow fluctuations in Au+Au collisions at $\sqrt{s_{NN}} = 200$ GeV are dominated by initial geometry fluctuations.

Intriguingly, whereas the values of $\sigma_{v_2}/\langle v_2 \rangle$ vary significantly as a function of centrality, the values of $\sigma_{v_3}/\langle v_3 \rangle$ are almost precisely 0.52 independent of centrality. To understand this better, we need to consider a rather peculiar feature of the Bessel-Gaussian Function. Figure 13 shows the $\sigma_{v_n}/\langle v_n \rangle$ of the Bessel-Gaussian as a function of the ratio δ/v_n^{RP}. For values of $\delta > v_n^{\mathrm{RP}}$, the observed $\sigma_{v_n}/\langle v_n \rangle$ saturates at a value of about 0.52. Thus, any Bessel-Gaussian in the large variance limit will have a $\sigma_{v_n}/\langle v_n \rangle$ of the same value.

This observation can, in fact, help shed light on the observed discrepancy between the CMS [11] and ATLAS [10] data on $\sigma_{v_3}/\langle v_3 \rangle$. Figure 14 shows $\sigma_{v_2}/\langle v_2 \rangle$ and $\sigma_{v_3}/\langle v_3 \rangle$ as a function of centrality in Pb+Pb collisions at $\sqrt{s_{NN}}$ = 2.76 TeV from CMS and ATLAS. The CMS results are obtained using the cumulant method assuming the small-variance limit. In contrast the ATLAS results are obtained via an event-by-event unfolding and calculating the exact mean and variance of the distribution.

The $\sigma_{v_2}/\langle v_2 \rangle$ values are in very good agreement, which appears to validate the small variance approximation (as was also validated in the Au+Au at $\sqrt{s_{NN}} = 200$ GeV case in this analysis). In contrast, there is a large difference in the $\sigma_{v_3}/\langle v_3 \rangle$ between the different methods. The ATLAS $\sigma_{v_3}/\langle v_3 \rangle$ values are all very close to 0.52, exactly as observed

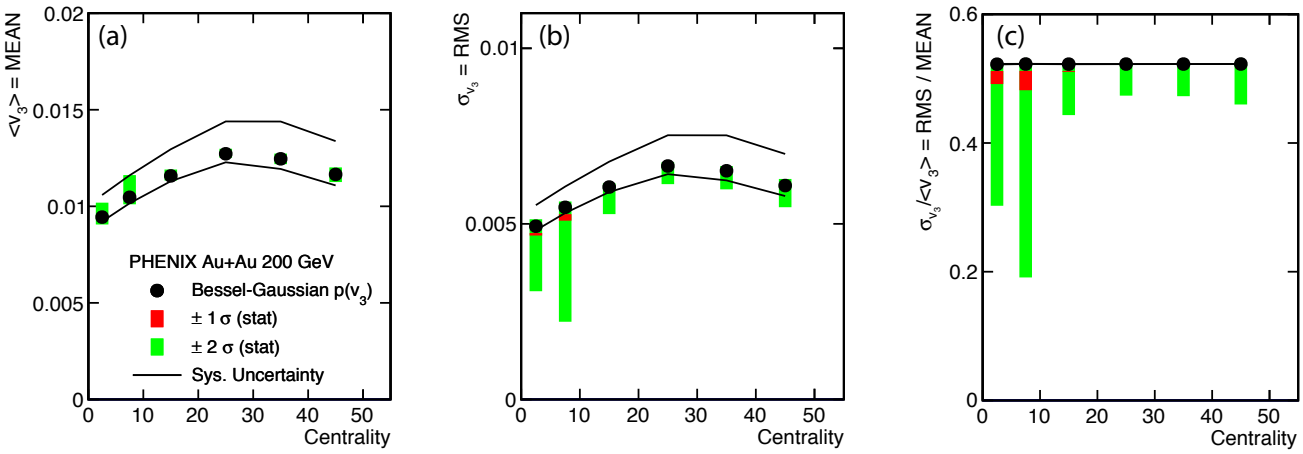

FIG. 12. Folding results for (a) $\langle v_3 \rangle$, (b) σ_{v_3}, and (c) $\sigma_{v_3}/\langle v_3 \rangle$. The black lines above and below the points indicate the systematic uncertainties. The red (green) boxes indicate the statistical uncertainties at the 68.27% (95.45%) confidence level. The $\sigma_{v_3}/\langle v_3 \rangle$ values are all ≈ 0.52, the apparent limiting value of this quantity for the Bessel-Gaussian distribution.

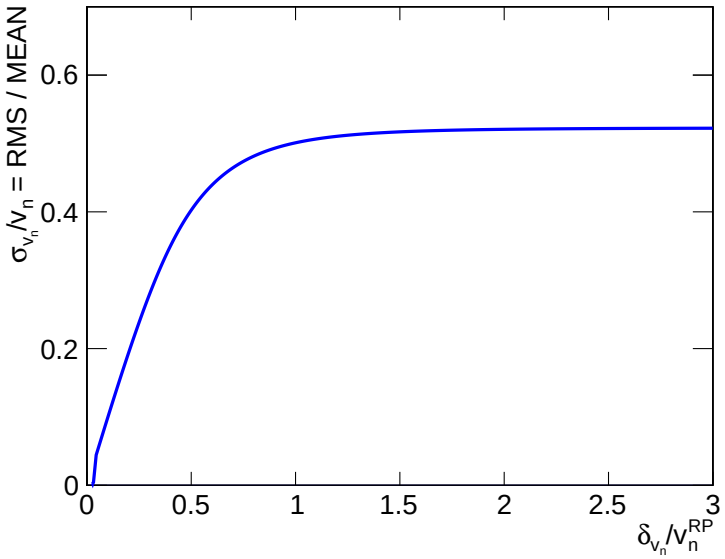

FIG. 13. The observed ratio of the mean to the standard deviation (i.e. $\sigma_{v_n}/\langle v_n \rangle$) of the Bessel-Gaussian as a function of the ratio of the two free parameters $\delta_{v_n}/v_n^{\rm RP}$. For values of $\delta_{v_n} > v_n^{\rm RP}$, the observed $\sigma_{v_n}/\langle v_n \rangle$ saturates at 0.52.

above in the present Au+Au data and as found to be a limiting case for the Bessel-Gaussian function. To better understand the $\sigma_{v_3}/\langle v_3 \rangle$, we also show $\sigma_{\varepsilon_3}/\langle \varepsilon_3 \rangle$ as determined from MC Glauber calculations. The dashed red-line uses the small-variance limit estimate with cumulants, as is done for the CMS data, and the agreement is quite reasonable. The solid red line is calculated from the moments of the ε_3 distribution directly, and shows good agreement with the ATLAS data. This represents a quantitative confirmation of the event-by-event fluctuations and the breakdown in the small variance approximation. The $v_3\{4\}$ at forward rapidity at RHIC is found to be complex-valued, which may be the result of a very small flow v_3 and significant nonflow contributions.

V. SUMMARY AND CONCLUSIONS

In summary, we have presented measurements of elliptic and triangular flow in Au+Au collisions at 200 GeV for charged hadrons at forward rapidity $1 < |\eta| < 3$. In particular, we compare flow cumulants ($v_2\{2\}$, $v_2\{4\}$, $v_2\{6\}$,

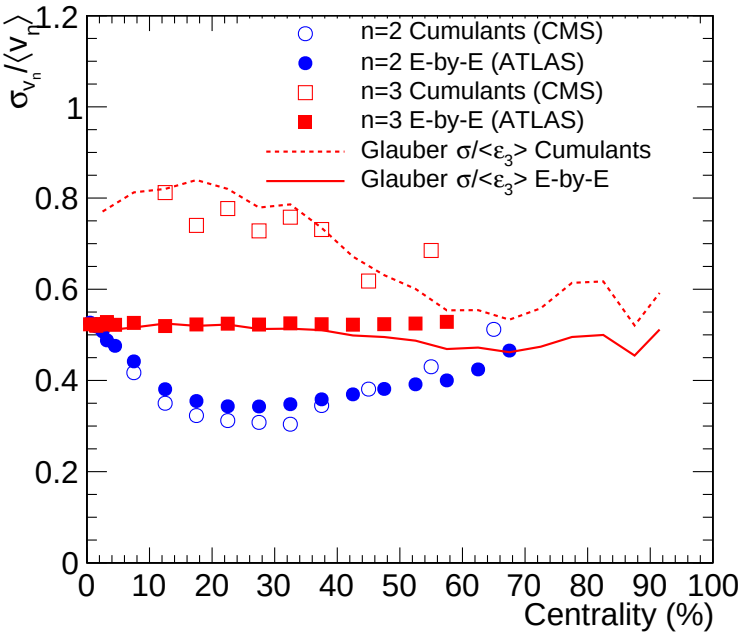

FIG. 14. The observed ratio of the standard deviation to the mean (i.e. $\sigma_{v_n}/\langle v_n \rangle$) for $n = 2$ and $n = 3$ as a function of centrality in Pb+Pb collisions at $\sqrt{s_{NN}} = 2.76$ TeV [10, 11]. Also shown are $\sigma_{\varepsilon_3}/\varepsilon_3$ values from MC Glauber estimated using the small-variance limit cumulant technique (shown as the dashed line) and the direct calculation from the moments (shown as the solid line).

$v_2\{8\}$ and $v_3\{2\}$, $v_3\{4\}$) and the mean and variance of the v_2 and v_3 event-by-event distributions using a forward-fold procedure with a Bessel-Gaussian ansatz. These measurements are complementary in terms of sensitivity to initial state geometry fluctuations and additional fluctuations from the evolution of the medium, for example via dissipative hydrodynamics.

In the small-variance limit, where the event-by-event flow fluctuations are small compared to the average flow value i.e. $\sigma_{v_n}/\langle v_n \rangle < 1$, we expect the cumulants extraction and the forward-fold results to agree. This is the case for elliptic flow in Au+Au collisions from 10%–50% central and both results agree with event-by-event fluctuations in the initial geometry as calculated via Monte Carlo Glauber.

In contrast, we find that the small-variance limit fails for triangular flow for all centralities at RHIC and the LHC. For LHC Pb+Pb results, the large-variance result for the cumulants can be described purely via Monte Carlo Glauber initial geometry fluctuations. However, for RHIC Au+Au collisions the complex values of $v_3\{4\}$ indicate that there may be additional nonflow influences as well as sources of fluctuations in the translation of initial geometry into final state momentum triangular anisotropies. Detailed comparisons with event-by-event hydrodynamic calculations should be elucidating to understand the nature of these fluctuations.

ACKNOWLEDGMENTS

We thank the staff of the Collider-Accelerator and Physics Departments at Brookhaven National Laboratory and the staff of the other PHENIX participating institutions for their vital contributions. We acknowledge support from the Office of Nuclear Physics in the Office of Science of the Department of Energy, the National Science Foundation, Abilene Christian University Research Council, Research Foundation of SUNY, and Dean of the College of Arts and Sciences, Vanderbilt University (U.S.A), Ministry of Education, Culture, Sports, Science, and Technology and the Japan Society for the Promotion of Science (Japan), Conselho Nacional de Desenvolvimento Científico e Tecnológico and Fundação de Amparo à Pesquisa do Estado de São Paulo (Brazil), Natural Science Foundation of China (People's Republic of China), Croatian Science Foundation and Ministry of Science and Education (Croatia), Ministry of Education, Youth and Sports (Czech Republic), Centre National de la Recherche Scientifique, Commissariat à l'Énergie Atomique, and Institut National de Physique Nucléaire et de Physique des Particules (France), Bundesministerium für Bildung und Forschung, Deutscher Akademischer Austausch Dienst, and Alexander von Humboldt Stiftung (Ger-

many), J. Bolyai Research Scholarship, EFOP, the New National Excellence Program (ÚNKP), NKFIH, and OTKA (Hungary), Department of Atomic Energy and Department of Science and Technology (India), Israel Science Foundation (Israel), Basic Science Research and SRC(CENuM) Programs through NRF funded by the Ministry of Education and the Ministry of Science and ICT (Korea), Physics Department, Lahore University of Management Sciences (Pakistan), Ministry of Education and Science, Russian Academy of Sciences, Federal Agency of Atomic Energy (Russia), VR and Wallenberg Foundation (Sweden), the U.S. Civilian Research and Development Foundation for the Independent States of the Former Soviet Union, the Hungarian American Enterprise Scholarship Fund, the US-Hungarian Fulbright Foundation, and the US-Israel Binational Science Foundation.

APPENDIX: TEST CASE FOR FULL UNFOLD

For this test case, the response matrix $\hat{A}$ is shown in Fig. 15 (a) and is identical to that for the real data 20%–30% centrality class. We then attempt to solve the inverse problem $\hat{A}\vec{Q}_2^{\rm true} = \vec{Q}_2^{\rm obs}$, where $Q_2^{\rm obs}$ has been obtained in the limit of infinite statistical precision, assuming a truth-level distribution with parameters such that the smearing, as encoded in $\hat{A}$, yields a distribution similar to that measured in data. The singular value factorization $\hat{A} = \hat{U}\hat{\Sigma}\hat{W}^T$ of the matrix is obtained, where $\hat{U}$ and $\hat{W}$ are unitary matrices whose column vectors, u_i and w_i, are the left- and right- singular vectors of $\hat{A}$, respectively, and $\hat{\Sigma}$ is a diagonal matrix, whose nonzero entries σ_i are its singular values. Figure 15 (b) shows a few selected right-singular vectors w_i. Notice that some vectors, namely those corresponding to the largest singular values, are harmonic, whereas those corresponding to the smallest singular values are essentially noise.

Because the response matrix is singular, we use the SVD decomposition to construct the solution of the inverse problem as a linear combination of *all* right-singular vectors, as follows:

$$\vec{Q}_2 = \sum_{i=1}^{\mathrm{Dim}(A)} \varphi_i \left(\frac{\vec{u}_i^T \cdot \vec{Q}_2^{\rm obs}}{\sigma_i} \right) \vec{w}_i. \tag{27}$$

The damping factors $\varphi_i = \sigma_i^2/(\sigma_i^2 + \lambda^2)$, for some $\lambda \in \mathbb{R}$, are introduced to attenuate the contribution of the noisy singular vectors to the sum. It is important to point out that in most implementations of SVD used in high-energy physics, including RooUnfold, the above sum is simply truncated to include only a subset of the harmonic singular vectors, potentially leading to loss of information.

To determine which singular vectors contribute to the solution in a meaningful manner, it is useful to examine the *Picard plot* [37] for the problem at hand, shown in Fig. 15 (c), which displays the singular values σ_i of $\hat{A}$, as well as the projection of $\vec{Q_2^{\rm obs}}$ onto the singular vectors $\vec{u}_i^T \cdot \vec{Q}_2^{\rm obs}$, and the solution coefficients $\vec{u}_i^T \cdot \vec{Q}_2^{\rm obs}/\sigma_i$. Notice that the singular values and the Fourier coefficients drop sharply many orders of magnitude before leveling off, yet in such a way that their ratio is roughly constant. The implication is then that all singular vectors appear to contribute equally to the solution, which is clearly problematic given the noisy nature of most of them. In general, it is desirable for Fourier coefficients to drop off faster than the singular values (to fulfill the so-called discrete Picard condition), such that the Picard plot will reveal the appropriate set of terms to include in the solution, as identified by a sharp drop in the solution coefficients.

Given that our problem does not satisfy the Picard condition, we introduce the attenuation factors φ_i in Eqn. 27. The resulting unfolded Q_2 is shown in Fig. 15 (d), along with the true $Q_2^{\rm true}$, and smeared $Q_2^{\rm obs}$. We observe that the unfolding works well, yielding a good description of the true distribution shape, with uncertainties associated with varying the regularization parameter λ.

However, in this case the unfolding procedure constitutes an ill-posed inverse problem, such that small perturbations in the input vector—that is, $Q_2^{\rm obs}$—translate to very large errors in the solution, compounded by the fact that the Picard condition is violated. In particular, we have verified with our test problem that the statistical fluctuations in $Q_2^{\rm obs}$ when sampling a *finite* number of events, comparable to those recorded in data, indeed limit the number of available harmonic singular vectors, thus causing the solution to be dominated by noise.

We now examine the application of the above unfolding method to data. Fig. 16 (a) shows an *ansatz* for $Q_2^{\rm true}$ assuming a Bessel-Gaussian form, and the corresponding refolded smeared distribution. It compares very well to the data, as shown in the ratio plot in Fig. 16 (b). In principle, given the good quality of the fit, one would expect the unfolding procedure to work with the data as input. However, the statistical fluctuations apparent in the ratio plot perturb the solution in such a way that the noisy nonharmonic singular vectors are enhanced even more than in the test problem, as shown in Fig. 16 (c). As a result, the number of available harmonic singular vectors is reduced, and the problem has no satisfactory solution, even when regularization is applied. Thus, to be explicit, the unfolding procedure fails. We note that if we apply our test example with a significantly better resolution, i.e. as in the ATLAS Pb+Pb case, the method does converge as expected.

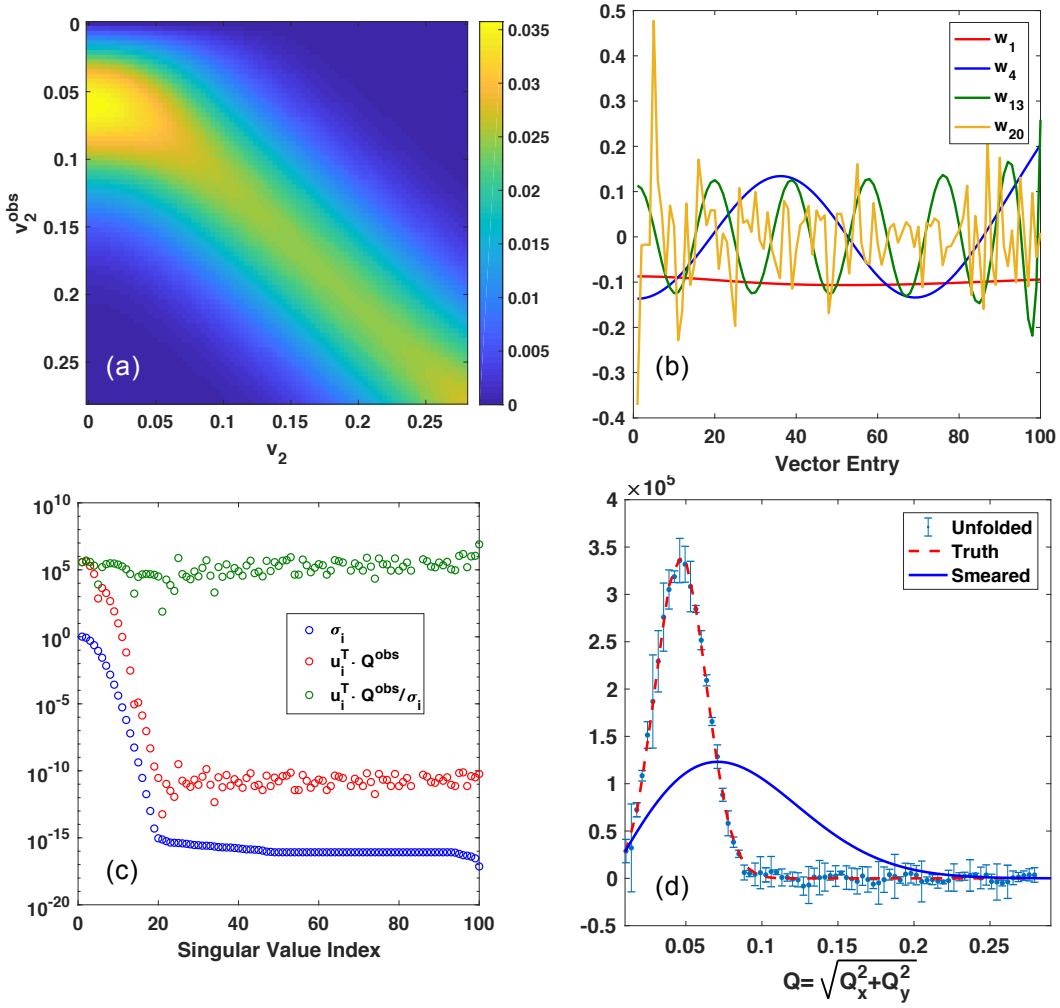

FIG. 15. (a) Response matrix for test unfolding problem; (b) Selected right-singular values of the response matrix; (c) Picard plot for inverse problem $\hat{A}\vec{Q}_2^{\rm true} = \vec{Q}_2^{\rm obs}$, see text for details; (d) True, smeared, and unfolded Q_2 as determined using SVD with attenuation factors.

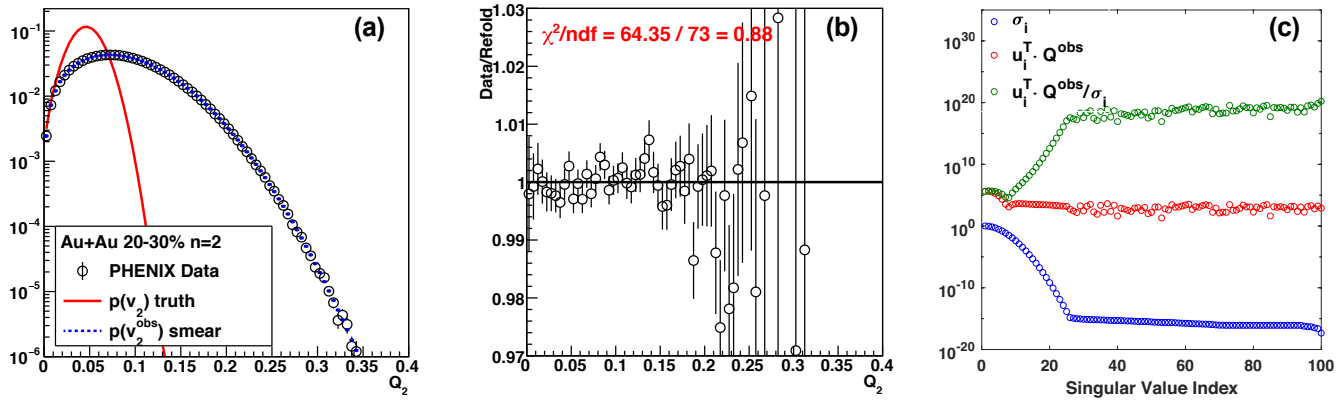

FIG. 16. (a) Data distribution for $Q_2^{\rm meas}$ in Au+Au collisions at $\sqrt{s_{NN}}$ = 200 GeV in the 20%–30% centrality class. Also shown is an assumed Bessel-Gaussian truth distribution and its resolution smeared result. (b) Data divided by the resolution smeared solution showing a good agreement within statistical uncertainties. (c) Picard plot for inverse problem with data $\hat{A}\vec{Q}_2^{\rm true} = \vec{Q}_2^{\rm obs}$, see text for details;

[1] K. Adcox *et al.* (PHENIX Collaboration), "Formation of dense partonic matter in relativistic nucleus-nucleus collisions at RHIC: Experimental evaluation by the PHENIX collaboration," Nucl. Phys. A **757**, 184 (2005).

[2] J. Adams *et al.* (STAR Collaboration), "Experimental and theoretical challenges in the search for the quark gluon plasma: The STAR Collaboration's critical assessment of the evidence from RHIC collisions," Nucl. Phys. A **757**, 102 (2005).

[3] B. B. Back *et al.* (PHOBOS Collaboration), "The PHOBOS perspective on discoveries at RHIC," Nucl. Phys. A **757**, 28 (2005).

[4] I. Arsene *et al.* (BRAHMS Collaboration), "Quark gluon plasma and color glass condensate at RHIC? The Perspective from the BRAHMS experiment," Nucl. Phys. A **757**, 1 (2005).

[5] P. Romatschke and U. Romatschke, "Relativistic Fluid Dynamics Out of Equilibrium," ArXiv:1712.05815.

[6] U. Heinz and R. Snellings, "Collective flow and viscosity in relativistic heavy-ion collisions," Ann. Rev. Nucl. Part. Sci. **63**, 123 (2013).

[7] S. A. Voloshin, A. M. Poskanzer, A. Tang, and G. Wang, "Elliptic flow in the Gaussian model of eccentricity fluctuations," Phys. Lett. B **659**, 537 (2008).

[8] J.-Y. Ollitrault, A. M. Poskanzer, and S. A. Voloshin, "Effect of flow fluctuations and nonflow on elliptic flow methods," Phys. Rev. C **80**, 014904 (2009).

[9] J. Jia, "Event-shape fluctuations and flow correlations in ultra-relativistic heavy-ion collisions," J. Phys. G **41**, 124003 (2014).

[10] G. Aad *et al.* (ATLAS Collaboration), "Measurement of the distributions of event-by-event flow harmonics in lead-lead collisions at = 2.76 TeV with the ATLAS detector at the LHC," J. High Energy Phys. **11 (2013)** 183.

[11] S. Chatrchyan *et al.* (CMS Collaboration), "Measurement of higher-order harmonic azimuthal anisotropy in PbPb collisions at $\sqrt{s_{NN}} = 2.76$ TeV," Phys. Rev. C **89**, 044906 (2014).

[12] J. Adams *et al.* (STAR Collaboration), "Azimuthal anisotropy in Au+Au collisions at $\sqrt{s_{NN}} = 200$ GeV," Phys. Rev. C **72**, 014904 (2005).

[13] B. Alver *et al.* (PHOBOS Collaboration), "Non-flow correlations and elliptic flow fluctuations in gold-gold collisions at $\sqrt{s_{NN}} = 200$ GeV," Phys. Rev. C **81**, 034915 (2010).

[14] K. Adcox *et al.* (PHENIX Collaboration), "PHENIX detector overview," Nucl. Instrum. Methods Phys. Res., Sec. A **499**, 469 (2003).

[15] M. Allen *et al.* (PHENIX Collaboration), "PHENIX inner detectors," Nucl. Instrum. Methods Phys. Res., Sec. A **499**, 549 (2003).

[16] C. Loizides, J. L. Nagle, and P. Steinberg, "Improved version of the PHOBOS Glauber Monte Carlo," SoftwareX **1-2**, 13 (2015).

[17] C. Aidala *et al.*, "The PHENIX Forward Silicon Vertex Detector," Nucl. Instrum. Methods Phys. Res., Sec. A **755**, 44 (2014).

[18] S. Agostinelli *et al.* (GEANT4 Collaboration), "GEANT4: A Simulation toolkit," Nucl. Instrum. Methods Phys. Res., Sec. A **506**, 250 (2003).

[19] S. A. Voloshin and Y. Zhang, "Flow study in relativistic nuclear collisions by Fourier expansion of Azimuthal particle distributions," Z. Phys. C **70**, 665 (1996).

[20] A. Bilandzic, R. Snellings, and S. Voloshin, "Flow analysis with cumulants: Direct calculations," Phys. Rev. C **83**, 044913 (2011).

[21] A. M. Poskanzer and S. A. Voloshin, "Methods for analyzing anisotropic flow in relativistic nuclear collisions," Phys. Rev. C **58**, 1671 (1998).

[22] N. Borghini, P. M. Dinh, and J.-Y. Ollitrault, "A New method for measuring azimuthal distributions in nucleus-nucleus collisions," Phys. Rev. C **63**, 054906 (2001).

[23] A. Bilandzic, C. H. Christensen, K. Gulbrandsen, A. Hansen, and Y. Zhou, "Generic framework for anisotropic flow analyses with multiparticle azimuthal correlations," Phys. Rev. C **89**, 064904 (2014).

[24] C. Adler *et al.* (STAR Collaboration), "Elliptic flow from two and four particle correlations in Au+Au collisions at $\sqrt{s_{NN}} = 200$ GeV," Phys. Rev. C **66**, 034904 (2002).

[25] J. Jia, M. Zhou, and A. Trzupek, "Revealing long-range multiparticle collectivity in small collision systems via subevent cumulants," Phys. Rev. C **96**, 034906 (2017).

[26] A. M Sirunyan *et al.* (CMS Collaboration), "Non-Gaussian elliptic-flow fluctuations in PbPb collisions at $\sqrt{s_{\rm NN}} = 5.02$ TeV," ArXiv:1711.05594.

[27] Z.-W. Lin, C. M. Ko, B.-A. Li, B. Zhang, and S. Pal, "A Multi-phase transport model for relativistic heavy ion collisions," Phys. Rev. C **72**, 064901 (2005).

[28] T. Adye, "Unfolding algorithms and tests using RooUnfold," in *Proceedings, PHYSTAT 2011 Workshop on Statistical Issues Related to Discovery Claims in Search Experiments and Unfolding, CERN,Geneva, Switzerland 17-20 January 2011*, CERN (CERN, Geneva, 2011) p. 313, arXiv:1105.1160 [physics.data-an].

[29] P. C. Hansen, "Truncated singular value decomposition solutions to discrete ill-posed problems with ill-determined numerical rank," SIAM J. Sci. Stat. Comput. **11**, 503 (1990).

[30] A. Hocker and V. Kartvelishvili, "SVD approach to data unfolding," Nucl. Instrum. Methods Phys. Res., Sec. A **372**, 469 (1996).

[31] M. Aaboud *et al.* (ATLAS Collaboration), "Measurement of long-range multiparticle azimuthal correlations with the

subevent cumulant method in pp and p+Pb collisions with the ATLAS detector at the CERN Large Hadron Collider," Phys. Rev. C **97**, 024904 (2018).
[32] B. B. Back *et al.* (PHOBOS Collaboration), "Centrality and pseudorapidity dependence of elliptic flow for charged hadrons in Au+Au collisions at $\sqrt{s_{NN}} = 200$ GeV," Phys. Rev. C **72**, 051901 (2005).
[33] J. Noronha-Hostler, L. Yan, F. G. Gardim, and J.-Y. Ollitrault, "Linear and cubic response to the initial eccentricity in heavy-ion collisions," Phys. Rev. C **93**, 014909 (2016).
[34] C. Aidala *et al.* (PHENIX Collaboration), "Measurements of Multiparticle Correlations in d + Au Collisions at 200, 62.4, 39, and 19.6 GeV and p + Au Collisions at 200 GeV and Implications for Collective Behavior," Phys. Rev. Lett. **120**, 062302 (2018).
[35] V. Khachatryan *et al.* (CMS Collaboration), "Evidence for collectivity in pp collisions at the LHC," Phys. Lett. B **765**, 193 (2017).
[36] L. Adamczyk *et al.* (STAR Collaboration), "Third Harmonic Flow of Charged Particles in Au+Au Collisions at sqrtsNN = 200 GeV," Phys. Rev. C **88**, 014904 (2013).
[37] P. C. Hansen, "The discrete picard condition for discrete ill-posed problems," BIT Numerical Mathematics **30**, 658 (1990).